PAPER

Check for updates

A multi-responsive chemosensor for highly sensitive and selective detection of Fe^{3+}, Cu^{2+}, $Cr_2O_7^{2-}$ and nitrobenzene based on a luminescent lanthanide metal–organic framework†

Yi Du, Huayong Yang, Ruijuan Liu, Caiyun Shao and Lirong Yang (iD) *

Excessive release of some hazardous chemicals, such as Fe^{3+}, Cu^{2+}, $Cr_2O_7^{2-}$ and nitrobenzene, may endanger public health and the environment; therefore, targeted effective sensing strategies are important. In this report, a series of lanthanide-based metal–organic frameworks (Ln-MOFs), namely $\{[Ln(dpc)(2H_2O)]\cdot(Hbibp)_{0.5}\}_n$ (H_4dpc = 2-(3′,4′-dicarboxylphenoxy) isophthalic acid, bibp = 4,4′-bis(imidazolyl) biphenyl, for **I–VI**, Ln = La, Ce, Pr, Nd, Sm, and Eu) were hydrothermally synthesized and characterized. Single-crystal X-ray diffraction indicates that **I–VI** are isostructural and the lanthanide center is nine-coordinated with a distorted tetrakaidecahedral configuration. The as-synthesized Ln-MOFs are assembled into three-dimensional frameworks through the connections of dpc^{4-} ligands and hydrogen bonding interactions. Notably, Eu-MOF (**VI**) behaves as a multi-responsive luminescent sensor toward Fe^{3+}, Cu^{2+}, $Cr_2O_7^{2-}$ and nitrobenzene with high sensitivity, selectivity, stability and anti-interference ability against the coexistence of other ions or molecules based on high luminescence quenching efficiency. Additionally, Eu-MOF (**VI**) shows excellent luminescence stability and retains its structural integrity within the pH range of 2–12 in an aqueous solution and its solid sample maintains high thermodynamic stability up to 320 °C. Furthermore, the possible luminescence sensing mechanisms have been discussed in detail, and are supported by PXRD analysis, UV-vis spectroscopy, X-ray photoelectron spectroscopy (XPS) or density functional theory (DFT).

Introduction

In recent decades, the ever-increasing unrestrained release of hazardous chemicals into the environment triggered by the rapid development of industry, agriculture, aquaculture and other anthropogenic activities has led to environmental problems due to the potential toxicity and nondegradability of the chemicals.[1–3] Therefore, it is extremely essential to establish analytical technologies and strategies for the detection, monitoring and removal of environmental pollutants such as harmful cations and anions, as well as toxic organic molecules, to reduce the risk of contamination.[4,5]

Iron(III), an essential element that plays vital functions in metabolic processes, such as hemoglobin formation, oxygen metabolism, and electron transfer, is widely distributed in the ecological system and environment. Both shortage and excess of iron may cause reduced immunity, iron deficiency anemia,

multiple organ failure and even esophageal cancer and bladder cancer, *etc*.[6–8] Copper(II), as another significant and indispensable ion, plays a critical role in living biological systems. However, excessive concentration of Cu^{2+} will pollute the environment and is harmful to human health, especially to the metabolism of the brain, which may lead to serious diseases, such as Alzheimer's disease and Wilson's disease.[9,10] Chromium, as a chemically toxic element, possesses extensive applications, such as in printing, electroplating, leather tanning, and some other industrial fields, and is a hazard to health and the environment.[11,12] Particularly, its hexavalent chromate anions (typically in the form of $Cr_2O_7^{2-}$) may lead to hereditary genetic defects, DNA damage, and carcinogenic and mutagenic effects that can potentially result in diverse types of cancers.[13,14] Nitrobenzene (NB), a compound that is a basic component of explosives, is widely used in many industrial processes including plastic manufacturing, pesticide production, aniline synthesis, *etc*. It has attracted particular attention due to its severe toxicity, carcinogenicity, nondegradability and cumulative effect.[15–17] Hence, developing rapid, effective, facile, low-cost, reliable, and environmental friendly technologies for sensing hazardous environmental contaminants with high selectivity and sensitivity is an urgent need to protect our health, food and the environment.[18,19]

Henan Key Laboratory of Polyoxometalate Chemistry, Institute of Molecular and Crystal Engineering, College of Chemistry and Chemical Engineering, Henan University, Kaifeng, Henan 475004, P. R. China. E-mail: lirongyang@henu.edu.cn
†Electronic supplementary information (ESI) available: CCDC 1817846, 1818344, 1835485, 1835486, 1835488 and 1887230. For ESI and crystallographic data in CIF or other electronic format see DOI: 10.1039/D0DT02120B

During the past decade, lanthanide metal–organic frameworks (Ln-MOFs), as potential functional crystalline materials, have attracted considerable attention due to their diversified structure, adjustable microporosity, and high surface area. Furthermore, Ln-MOFs have the inherent optical features of wide photoluminescent energy gaps, characteristic emission bands, long luminescence lifetimes, high color purity, large Stokes shift, visible luminescent colors, *etc.*, which are essentially derived from f–f transitions through the "antenna effect" enhanced by suitable organic ligands. In view of these characteristics, Ln-MOFs may act as promising chemical sensing materials toward certain environmental contaminants.[20–25]

Commonly, multidentate ligands like polyaromatic acids are potential linkers for self-assembling MOFs derived from their architectural features as follows: (1) polyaromatic acid may deprotonate in different degrees at regulated pH values and facilitate the construction of multidimensional MOFs; (2) being a π-electron rich ligand, 2-(3′,4′-dicarboxylphenoxy)isophthalic acid may serve as an eminent luminescent chromophore or "antenna" to sensitize the luminescence and enhance the bright emission of Ln-MOFs, which may endow them with luminescent multifunctionality; (3) polyaromatic acid ligands may provide uncoordinated carboxyl oxygen atoms as exposed active sites to capture certain trace analytes; (4) they can promptly release a signal when the combination occurs between the π-conjugated rings of polyaromatic acids and the target analytes through π–π interactions and/or other weak interactions, which may motivate the high sensing sensitivity of Ln-MOFs.[26–29] Based on the aforementioned considerations, a series of Ln-MOFs with mixed ligands, namely $\{[Ln(dpc)(2H_2O)]\cdot(Hbibp)_{0.5}\}_n$ have been synthesized and characterized. Particularly, Eu-MOF (**VI**) acts as a multi-responsive luminescent sensor toward Fe^{3+}, Cu^{2+}, $Cr_2O_7^{2-}$, and nitrobenzene with high sensitivity, selectivity and stability, and shows anti-interference from the corresponding ions or molecules.

Experimental section

Materials and methods

All raw materials and solvents (AR grade) were purchased commercially and used without any further purification. FT-IR spectra were recorded on an AVATAR 360 FT-IR spectrometer in the range of 4000–400 cm^{-1} with a powder sample on KBr pellets. Powder X-ray diffraction (PXRD) patterns were collected on a Bruker D8 Advance instrument with Cu-Kα radiation (λ = 1.54056 Å) in the range of 2θ = 5–50° at room temperature. Elemental analyses for C, H and N were performed on a PerkinElmer 240 CHN elemental analyzer. Thermogravimetric analyses (TGA) were done on a PerkinElmer TGA7 thermogravimeter from ambient temperature to 1000 °C in the protecting stream of a N_2 flow at a heating rate of 10 °C min^{-1}. All luminescence spectra were obtained on an Edinburgh FLS 980 spectrophotometer equipped with a 450 W xenon lamp and UF900H high-energy microsecond flashlamp as the excitation sources at room temperature. Fe^{3+}@Eu-MOF and Cu^{2+}@Eu-

MOF were determined by using an Optima DV2100 inductively coupled plasma-atomic emission spectrometer (ICP-AES, PerkinElmer). X-ray photoelectron spectra (XPS) were obtained on a Thermo Scientific ESCALAB 250Xi X-ray photoelectron spectrometer. All UV-vis spectra were acquired from a TU-1900 spectrometer at room temperature.

Synthesis of $\{[Ln(dpc)(2H_2O)]\cdot(Hbibp)_{0.5}\}_n$ (I–VI)

A mixture of $Ln(NO_3)_3\cdot6H_2O$ (0.075 mmol), H_4dpc (0.1 mmol) and bibp (0.1 mmol) in 15 mL H_2O was stirred for 40 min and then transferred into a 25 mL Teflon-lined stainless steel autoclave at 130 °C for 72 h. After cooling to room temperature at a rate of 5 °C h^{-1}, yellowish cluster crystals were obtained. Ln-MOFs of **I–VI** were synthesized under similar conditions. The analysis data of **I–VI** are listed in detail as follows:

$\{[La(dpc)(2H_2O)]\cdot(Hbibp)_{0.5}\}_n$ (**I**). Yields: 47.25% (based on La). Anal. calcd for $C_{25}H_{18}LaN_2O_{11}$ (M_r = 661.32): C, 45.47; H, 2.60; N, 4.24. Found: C, 44.47; H, 2.65; N, 4.13%. IR (KBr, cm^{-1}): 3123 (br), 1928 (w), 1656 (s), 1593 (s), 1553 (s), 1460 (w), 1375 (s), 1309 (w), 1268 (m), 1233 (m), 1117 (m), 1078 (m), 952 (m), 862 (m), 823 (m), 776 (w), 704 (s), 676 (w), 622 (m), 543 (m), 511 (w), 469 (m).

$\{[Ce(dpc)(2H_2O)]\cdot(Hbibp)_{0.5}\}_n$ (**II**). Yields: 43.15% (based on Ce). Anal. calcd for $C_{25}H_{18}CeN_2O_{11}$ (M_r = 662.53): C, 45.39; H, 2.59; N, 4.23. Found: C, 45.37; H, 2.55; N, 4.32%. IR (KBr, cm^{-1}): 3123 (br), 1918 (w), 1658 (s), 1592 (s), 1552 (s), 1515 (s), 1468 (m), 1377 (s), 1312 (s), 1268 (m), 1232 (m), 1162 (w), 1056 (w), 953 (m), 862 (m), 823 (m), 776 (w), 705 (s), 662 (w), 632 (m), 535 (m), 496 (w), 462 (w).

$\{[Pr(dpc)(2H_2O)]\cdot(Hbibp)_{0.5}\}_n$ (**III**). Yields: 46.43% (based on Pr). Anal. calcd for $C_{25}H_{18}PrN_2O_{11}$ (M_r = 663.32): C, 45.34; H, 2.59; N, 4.23. Found: C, 45.44; H, 2.61; N, 4.21%. IR (KBr, cm^{-1}): 3129 (br), 1916 (w), 1658 (s), 1602 (s), 1550 (s), 1513 (s), 1463 (m), 1378 (s), 1302 (s), 1268 (m), 1231 (m), 1155 (w), 1058 (w), 953 (m), 859 (m), 823 (m), 766 (w), 705 (s), 672 (w), 632 (m), 545 (m), 514 (w), 471 (w).

$\{[Nd(dpc)(2H_2O)]\cdot(Hbibp)_{0.5}\}_n$ (**IV**). Yields: 42.18% (based on Nd). Anal. calcd for $C_{25}H_{18}NdN_2O_{11}$ (M_r = 666.65): C, 45.11; H, 2.57; N, 4.21. Found: C, 45.15; H, 2.62; N, 4.17%. IR (KBr, cm^{-1}): 3128 (br), 1923 (w), 1658 (s), 1602 (s), 1551 (s), 1516 (s), 1463 (w), 1378 (s), 1319 (w), 1268 (m), 1231 (m), 1167 (m), 1058 (m), 953 (m), 860 (m), 823 (m), 766 (w), 705 (s), 666 (w), 632 (m), 533 (m), 491 (w), 471 (m).

$\{[Sm(dpc)(2H_2O)]\cdot(Hbibp)_{0.5}\}_n$ (**V**). Yields: 47.35% (based on Sm). Anal. calcd for $C_{25}H_{18}SmN_2O_{11}$ (M_r = 672.76): C, 44.70; H, 2.55; N, 4.17. Found: C, 43.72; H, 2.84; N, 4.12%. IR (KBr, cm^{-1}): 3127 (br), 1918 (w), 1657 (s), 1602 (s), 1552 (s), 1512 (s), 1463 (w), 1404 (s), 1379 (s), 1319 (w), 1269 (m), 1231 (m), 1167 (m), 1059 (w), 953 (m), 861 (m), 823 (m), 766 (w), 706 (s), 686 (w), 633 (m), 533 (m), 492 (w), 472 (w).

$\{[Eu(dpc)(2H_2O)]\cdot(Hbibp)_{0.5}\}_n$ (**VI**). Yields: 56.69% (based on Eu). Anal. calcd for $C_{25}H_{18}EuN_2O_{11}$ (M_r = 674.37): C, 44.59; H, 2.54; N, 4.16. Found: C, 44.61; H, 2.57; N, 4.11%. IR (KBr, cm^{-1}): 3122 (br), 1923 (w), 1658 (s), 1595 (s), 1555 (s), 1515 (s), 1468 (m), 1379 (s), 1305 (m), 1268 (m), 1236 (m), 1156 (m),

Table 1 Crystallographic data and structure refinement details for **I–VI**

Compound	I	II	III	IV	V	VI
Empirical formula	$C_{25}H_{18}LaN_2O_{11}$	$C_{25}H_{18}CeN_2O_{11}$	$C_{25}H_{18}PrN_2O_{11}$	$C_{25}H_{18}NdN_2O_{11}$	$C_{25}H_{18}SmN_2O_{11}$	$C_{25}H_{18}EuN_2O_{11}$
Formula weight	661.32	662.53	663.32	666.65	672.76	674.37
Temperature/K	273(2)	296(2)	296(2)	296(2)	296(2)	296(2)
Crystal system	Monoclinic					
Space group	$P2_1/c$					
a/Å	16.398(8)	16.2883(10)	16.097(5)	16.2535(18)	16.2397(14)	16.213(3)
b/Å	8.627(4)	8.5827(5)	8.503(3)	8.5688(9)	8.5555(7)	8.5404(14)
c/Å	19.391(9)	19.2359(12)	19.088(6)	19.213(2)	19.2033(17)	19.151(4)
β/(°)	115.01	114.7250(9)	114.725(4)	114.7074(16)	114.7534(12)	114.685(3)
Volume/Å^3	2486(2)	2442.6(3)	2373.2(13)	2430.9(5)	2422.9(4)	2409.4(8)
Z	4					
ρ_{calc}/g cm^{-3}	1.767	1.802	1.857	1.822	1.844	1.859
μ/mm^{-1}	1.785	1.932	2.123	2.204	2.492	2.672
$F(000)$	1308	1312	1316	1320	1328	1332
Crystal size/mm^3	0.14 × 0.10 × 0.07	0.40 × 0.22 × 0.07	0.36 × 0.23 × 0.07	0.40 × 0.17 × 0.06	0.44 × 0.26 × 0.06	0.08 × 0.07 × 0.05
2θ range	4.64–38.74	4.66–56.54	5.34–57.22	5.30–56.90	4.32–56.48	5.32–33.64
Index ranges	$-21 \leq h \leq 21$, $-11 \leq k \leq 10$, $-13 \leq l \leq 25$	$-19 \leq h \leq 21$, $-11 \leq k \leq 11$, $-24 \leq l \leq 24$	$-21 \leq h \leq 16$, $-11 \leq k \leq 10$, $-22 \leq l \leq 25$	$-21 \leq h \leq 21$, $-11 \leq k \leq 11$, $-16 \leq l \leq 25$	$-21 \leq h \leq 18$, $-10 \leq k \leq 11$, $-24 \leq l \leq 24$	$-21 \leq h \leq 21$, $-11 \leq k \leq 10$, $-25 \leq l \leq 18$
Reflections collected	15 227	15 164	14 902	15 058	14 632	14 806
Independent reflections	5762 [R_{int} = 0.0996, R_{sigma} = 0.1340]	5972 [R_{int} = 0.0342, R_{sigma} = 0.0462]	5894 [R_{int} = 0.0367, R_{sigma} = 0.0474]	5981 [R_{int} = 0.0357, R_{sigma} = 0.0458]	5862 [R_{int} = 0.0388, R_{sigma} = 0.0517]	796 [R_{int} = 0.1233, R_{sigma} = 0.1691]
Data/restraints/parameters	5762/0/353	5972/0/352	5894/0/352	5981/0/352	5862/0/352	5796/18/342
Goodness-of-fit on F^2	0.933	1.012	1.043	1.031	1.072	0.940
R_1, wR_2 [$I > 2\sigma(I)$]	0.0534/0.0940	0.0280/0.0592	0.0254/0.0657	0.0257/0.0589	0.0323/0.0895	0.0600/0.1018
R_1, wR_2 [all data]	0.1056/0.1127	0.0386/0.0637	0.0279/0.0673	0.0324/0.0621	0.0376/0.0931	0.1330/0.1291

1059 (m), 955 (m), 898 (w), 823 (m), 788 (m), 704 (m), 666 (w), 622 (m), 560 (w), 514 (w), 465 (w).

Crystallographic data collection and refinement

Single-crystal X-ray diffraction data of **I–VI** were obtained on a Bruker Smart CCD X-ray single-crystal diffractometer with graphite monochromated MoKα-radiation (λ = 0.71073 Å). All structures were solved by direct methods and Fourier synthesis. Positional and thermal parameters were refined by the full-matrix least-squares method on F^2 using the SHELXTL software package. The pertinent crystallographic data and structure refinement parameters for Ln-MOFs **I–VI** are listed in Table 1. The selected bond lengths and angles of **I–VI** are given in Table S1.† CCDC reference numbers for MOFs **I–VI** are 1887230, 1835485, 1817846, 1835486, 1818344 and 1835488, respectively.†

Results and discussion

Description of the crystal structures

Single-crystal X-ray diffraction demonstrates that **I–VI** are isomorphous and isostructural, crystallizing in the monoclinic space group $P2_1/c$. **I–VI** display similar IR spectra in the range of 4000–400 cm^{-1} based on their similar structural characteristics. The bands from 1590 to 1550 cm^{-1} correspond to the COO^- asymmetric symmetric stretching vibrations ($\nu_{as}COO^-$) and the COO^- symmetry stretching vibrations ($\nu_s COO^-$) ranging from 1400 to 1370 cm^{-1}. Herein, Eu-MOF (**VI**) is selected as a representative to describe the assembly process of the 3D structure in detail. The asymmetric unit of **VI** contains one crystallographically independent Eu(III) ion. In the Eu-MOF, the Eu1(III) center is nine-coordinated with a distorted tetrakaidecahedral coordination configuration defined by seven oxygen atoms (O1, O4, O5, O6, O6a, O7 and O9) derived from four dpc^{4-} ligands and two coordinated water molecules (O1 W and O2 W) to form a {EuO$_9$} unit (as shown in Fig. 1a). Around Eu1, four dpc^{4-} ligands adopt the coordination mode of μ_4-η^1,η^1,η^1,η^2,η^1,η^1 (see Scheme 1). Under the synergistic effect of deprotonated carboxyl oxygen atoms and protonated nitrogen atoms provided by the auxiliary ligand bibp, Eu-MOF (**VI**) maintains charge balance. The Eu1–O$_{carboxyl}$ bond lengths fall into the 2.293(6)–2.576(6) Å range, whereas those of Eu1–OW vary from 2.487(6) to 2.518(6) Å, which are consistent with those observed in the reported lanthanide compounds.[30,31] It is noticeable that two neighbouring Eu(III) centers are bridged by two carboxylate groups adopting the mode of μ_2-η^1,η^2 to form a binuclear europium-
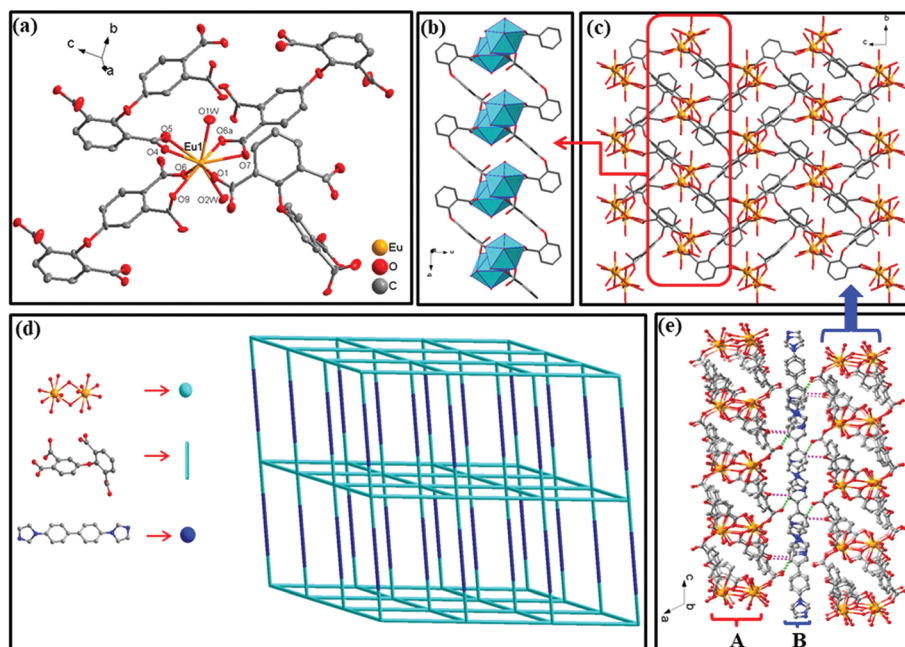
Fig. 1 (a) Coordination environment of the Eu(III) center in Eu-MOF. (b) 1D wavy chain in the Eu-MOF. (c) 2D architecture in the Eu-MOF. (d) The network topology of the Eu-MOF. (e) The hydrogen bonds between two styles of layers in the Eu-MOF (type A and B) (hydrogen atoms are omitted for clarity).
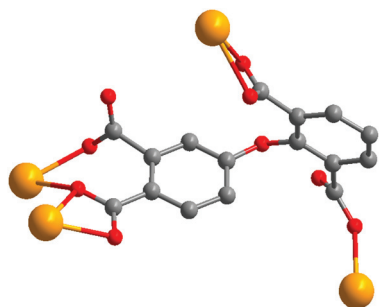
Scheme 1 The coordination mode of the dpc^{4-} ligand in Ln-MOFs **I–VI**.

carboxylate cluster of $[Eu(COO)_2Eu]$ (with a Eu1⋯Eu1 non-bonding distance of 4.2202(10) Å) as a building block, upon which a secondary building unit (SBU) involving an ${EuO_9}_2$ edge-sharing polyhedron is formed. Afterwards, the SBUs are linked to extend an infinite chain architecture running along a direction through dpc^{4-} ligands (Fig. 1b). The adjacent chains are further reciprocally connected to a 2D layer (type A) along a direction by the dpc^{4-} ligands (as illustrated in Fig. 1c). Interestingly, one layer of uncoordinated bibp (type B) ligands is sandwiched between two adjoining layers (type A). Both types of layers are further interlinked alternately in $(\cdots A–B–A–B\cdots)_n$ style to give rise to a 3D supramolecular framework through hydrogen bond interactions (see Fig. 1e and Table S2†), and the network topology of the Eu-MOF is shown in Fig. 1d. By comparison and analysis based on their crystallographic parameters, the lanthanide contraction effect is authenticated. The average distances of Ln–$O_{carboxyl}$, Ln–OW and Ln⋯Ln in **I–VI** decrease regularly according to the order of La, Ce, Pr, Nd, Sm and Eu, which is ascribed to the crystal field contractions of the rare earth elements due to the lack of spherical symmetry. The corresponding data are listed in Table S3.†

Thermogravimetric analyses and powder X-ray diffraction

The thermal stability of Ln-MOFs **I–VI** is confirmed by thermogravimetric analysis within the temperature range of 30–1000 °C under a N_2 atmosphere. The TG curves of **I–VI** display analogous behavior, in accordance with their similar structures and isomorphism (see Fig. S1†). Herein, the Eu-MOF was selected as a representative example to describe their weight loss processes in detail. According to the TG curve, the Eu-MOF undergoes two steps of weight loss: the first step occurs within the temperature range of 30 to 180 °C, attributed to the evacuation of two coordination water molecules (obsd: 5.23%; calcd: 5.35%). The main framework can remain stable up to 320 °C. Upon further heating, it begins to collapse with the loss of organic ligands, demonstrating that the framework of the Eu-MOF successively decomposes.

Meanwhile, the experimental PXRD patterns of Ln-MOFs **I–VI** are in good agreement with those of the simulated ones based on the crystallographic data, respectively, which confirm the phase purity of **I–VI** (Fig. S2†). To corroborate the chemical stability of **I–VI**, the samples were immersed in aqueous solutions of pH = 2–12 for 48 hours and then centrifuged to obtain XRD-testable samples at ambient temperature. Interestingly, under different pH conditions, the emission spectra of the Eu-
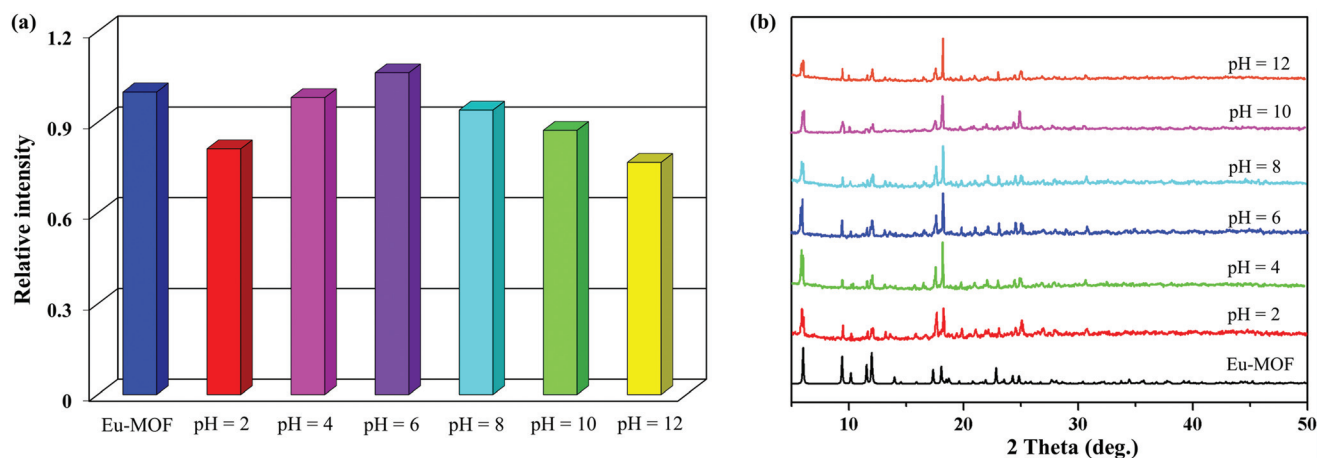
Fig. 2 (a) Luminescence intensities of the Eu-MOF ($^5D_0 \rightarrow {}^7F_2$) at different pH values of 2–12. (b) The PXRD of the Eu-MOF soaked in aqueous solutions with different pH values.

MOF ($^5D_0 \rightarrow {}^7F_2$) still possess luminescence stability and the results of PXRD accord with the simulated pattern from the crystallographic data (Fig. 2), indicating that the Eu-MOF can withstand acidic/basic conditions and maintain the integrity of the framework in a wide range of pH values. The high stability of the Eu-MOF in the aqueous system may arise from the following reasons: (1) a stronger coordination bond between carboxylic oxygen atoms and Eu(III) centers; (2) the infinite and close-knit [Eu(COO)$_2$Eu]$_n$ chain and a higher dense 3D framework; (3) hydrogen bond interactions further stabilize the 3D skeleton. As a result, the stability of the Eu-MOF is enhanced synergistically by the three factors.[32–35] Apparently, in view of its prominent chemical stability, the Eu-MOF is endowed with advantageous opportunities as a chemosensor for certain analytes.

Luminescence properties

MOFs based on certain Ln(III) ions can show excellent luminescence properties originating from the nature of 4f electrons, especially those of Eu-MOFs. The solid state luminescence properties of the isolated H$_4$dpc ligand and Eu-MOF were studied at room temperature. The free H$_4$dpc ligand possesses a broad emission band at 420 nm (λ_{ex} = 339 nm) (Fig. S4†), which could be ascribed to the $\pi \rightarrow \pi^*$ or n $\rightarrow \pi^*$ transitions.[36,37] On monitoring at 616 nm, the excitation spectrum of the Eu-MOF consists of three main peaks, where the wide band of 250–350 nm is attributable to the $\pi \rightarrow \pi^*$ electronic transition of the organic ligand, while the leftover narrow bands can be attributed to the energy level transition of the Eu(III) ion. The emission spectrum of the Eu-MOF was measured at an excitation wavelength of 296 nm; in the monitored emission spectrum, the characteristic $^5D_0 \rightarrow {}^7F_j$ (j = 1–4) transition of Eu(III) locates at 592, 616, 652, 700 nm, and the ligand emission was not observed in the Eu-MOF, which indicates that the dpc^{4-} ligand acts as an "antenna chromophore" and effective energy transfer between the ligand and Eu(III) ion occurs.[38–40] The

$^5D_0 \rightarrow {}^7F_1$ transition for the Eu-MOF at 592 nm implies the magnetic-dipole transition and it's practically uninfluenced by the ligand field. A typical electric-dipole transition of $^5D_0 \rightarrow {}^7F_2$, called the hypersensitive transition, suggests that the Eu(III) ion is located at positions where there is no reverse symmetry and leads to the glaring red luminescence of the Eu-MOF. By comparison, the emission intensity of the $^5D_0 \rightarrow {}^7F_2$ transition is much higher than that of the $^5D_0 \rightarrow {}^7F_1$ transition and the ratio of $I(^5D_0 \rightarrow {}^7F_2)/I(^5D_0 \rightarrow {}^7F_1)$ is 11.78, indicating that the coordination environment of Eu(III) occupies a low-symmetry environment with no inversion center and matches well with the results of the single-crystal X-ray analysis.[41–43] There exists a weak emission band at 652 nm pertaining to the $^5D_0 \rightarrow {}^7F_3$ transition. According to the CIE chromaticity diagram, the CIE color coordinates of the Eu-MOF lie in (0.613, 0.311), as shown in Fig. 3b, which is consistent with the bright red emission visibly observed with the naked eye under 365 nm UV irradiation (see the inset in Fig. 3a), demonstrating the occurrence of the "antenna effect" ulteriorly. Additionally, we also monitored the emissions of the $^5D_0 \rightarrow {}^7F_2$ transition for the Eu-MOF to measure its emission decay lifetime (Fig. S5†). The transient decay curve of the Eu-MOF agrees well with the mono-exponential function: $I = A \exp(t/\tau)$, and the value of the decay time is 357 μs.

Sensing of organic solvent molecules

A consideration of the prominent chemical stabilities and the characteristic bright red luminescence of the Eu-MOF in this work inspires us to explore its potential applications. To investigate the sensing ability of the Eu-MOF for organic molecules, finely ground crystalline samples (2 mg each) were dispersed into different organic solvents (3 mL), kept standing for three days and then ultrasonicated for 30 min at ambient temperature to obtain stable suspensions. The corresponding characteristic emission curves of the Eu-MOF in different solvents are shown in Fig. 4a, and the highest emission peak at 616 nm ($^5D_0 \rightarrow {}^7F_2$) was monitored to determine their emission inten-
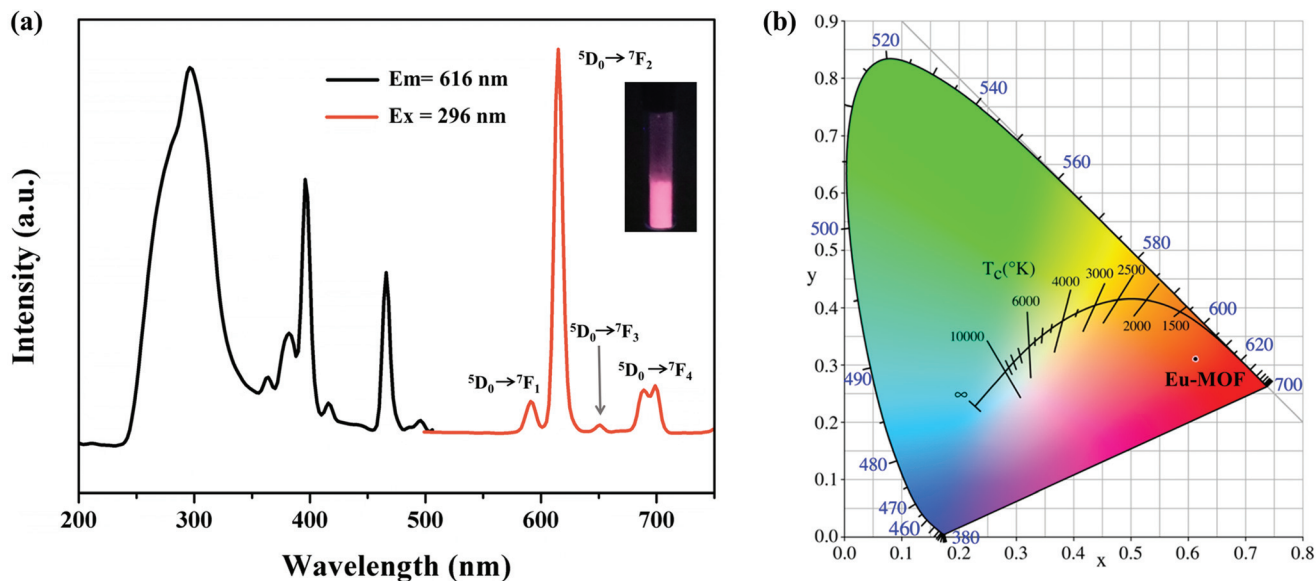
Fig. 3 (a) Excitation (black line) and emission spectra of the Eu-MOF (inset: luminescence picture under UV-light irradiation at 365 nm). (b) The corresponding CIE chromaticity diagram.
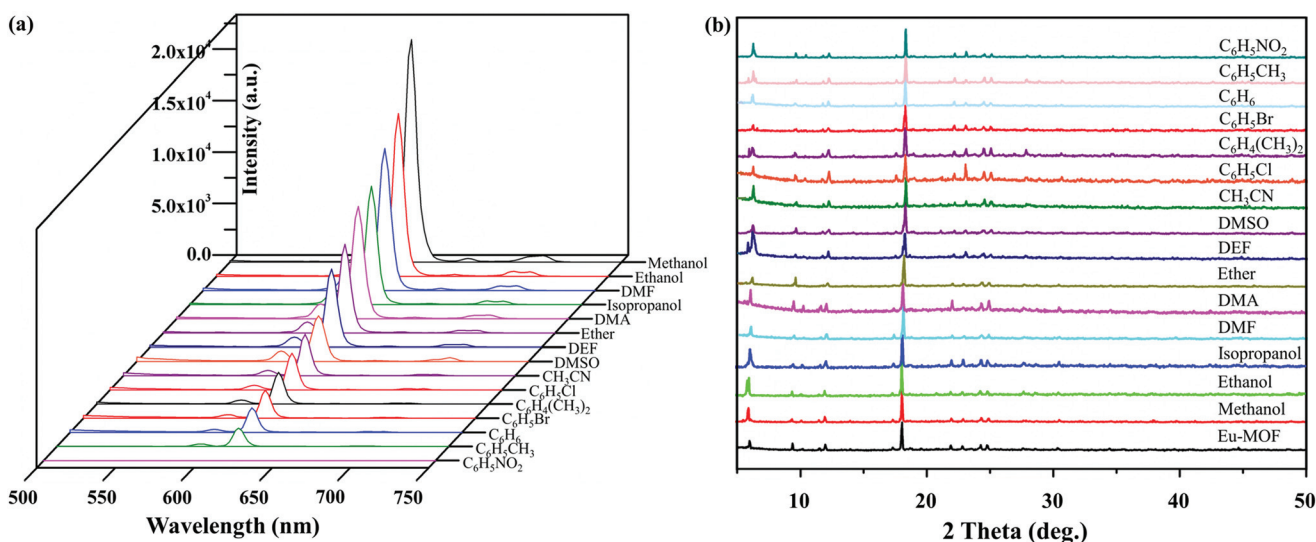

Fig. 4 (a) Emission spectra of the Eu-MOF in different organic solvents. (b) The XRD patterns of the Eu-MOF after the detection of organic molecules.

sities. Various solvents have different effects on the luminescence of Eu-MOF. Interestingly, the luminescence intensity of the Eu-MOF exhibits a remarkable quenching effect when the crystalline sample is dispersed into $C_6H_5NO_2$ (NB), while other luminescence intensities are largely dependent upon the corresponding solvents, and the order of the luminescence intensities is: methanol > ethanol > DMF > isopropanol > DMA > ether > DEF > DMSO > CH_3CN > C_6H_5Cl > $C_6H_4(CH_3)_2$ > C_6H_5Br > C_6H_6 > $C_6H_5CH_3$ > $C_6H_5NO_2$. Furthermore, the stability of the Eu-MOF in various solvents was also evaluated by PXRD (as shown in Fig. 4b), indicating that the integrity of the

framework remains unchanged in the tested chemical reagents and the Eu-MOF can be used as a candidate material for luminescent probes.

To further explore the relationship of concentration-dependent luminescence intensity, luminescence titration experiments were performed by gradual addition of NB (5×10^{-2} M) in DMF solutions, respectively. As the concentration of NB in DMF gradiently increased, the luminescence intensities of the Eu-MOF decreased gradually and even almost completely quenched. When the volume of NB is added to 200 μL, the quenching efficiency (QE), calculated using $(I_0 - I)/I_0 \times 100\%$,
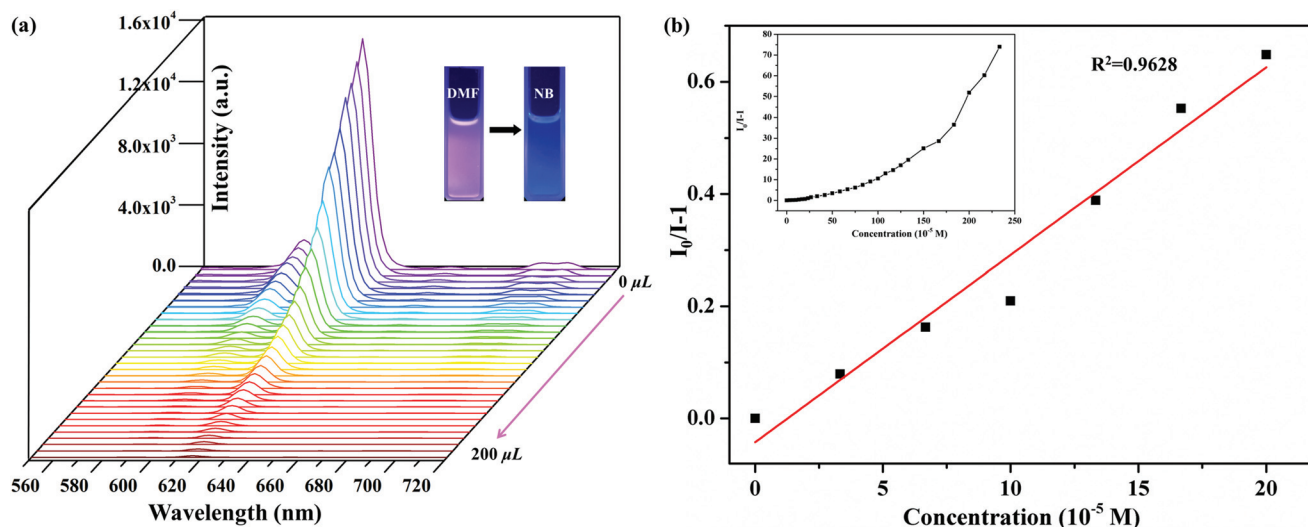
Fig. 5 (a) Concentration-dependent luminescence intensities of the Eu-MOF by the addition of different volumes of NB (5×10^{-2} M). (b) Linear SV curve for NB (inset: nonlinear SV curve of analytes).

comes up to 98.98% (Fig. 5a). The luminescence quenching efficiency was analyzed by using the Stern–Volmer (SV) equation: $I_0/I = K_{sv}[A] + 1$, where K_{sv} is defined as the quenching constant (M^{-1}), I_0 and I represent the luminescence intensities of the Eu-MOF before and after the introduction of the analytes in DMF solutions, and [A] is the molar concentration of the analytes. The SV plot for NB is nearly linear at low concentrations (with a correlation coefficient of $R^2 = 0.9628$) (Fig. 5b), however, as the concentration increases, it no longer conforms to the linear equation which can be attributed to the energy-transfer process and self-absorption.[44,45] The quenching constant (K_{sv}) for NB is calculated to be 3.34×10^3 M^{-1}. Based on the formula of $3\delta/k$ (δ: standard error, k: slope derived from the linear regression of I vs. [NB] at low concentration range), the limit of detection (LOD) for NB is calculated

as 2.89×10^{-5} M, demonstrating that the Eu-MOF is highly sensitive to NB.

Furthermore, the interference experiments of other solvents on NB were studied. The sample of the Eu-MOF was separately dispersed in DMF solution with different organic solvents, and sonicated to form a stable suspension, and the emission intensity was tested under excitation at 296 nm. As shown in Fig. 6a, the luminescence intensities of the Eu-MOF changed slightly after the mere addition of other organic solvents, whereas those of the Eu-MOF declined sharply with the introduction of 300 μL NB (1×10^{-2} M), indicating that the Eu-MOF has excellent selectivity for detecting NB. To test the recyclable performance of the Eu-MOF for NB, the Eu-MOF was immersed in DMF containing NB to prepare the NB@Eu-MOF sample, and then washed five times with fresh DMF and centrifuged to
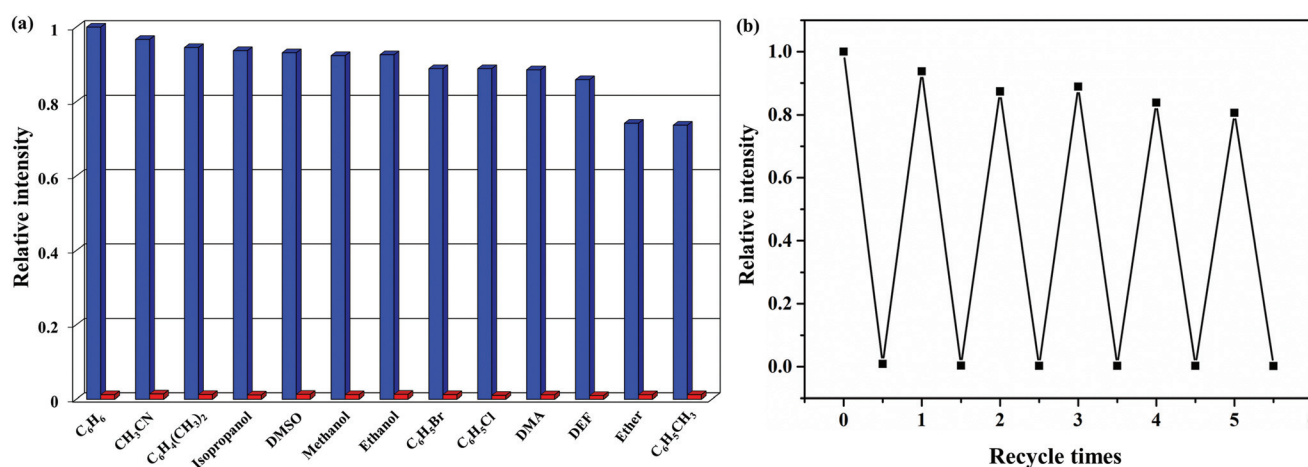

Fig. 6 (a) Comparison of the luminescence intensity ($^5D_0 \rightarrow {}^7F_2$, 616 nm) of the Eu-MOF in sensing NB with the interference of different organic solvents, the red and blue columns represent the presence and absence of NB, respectively. (b) The quenching and recovery tests of the Eu-MOF for NB in DMF.
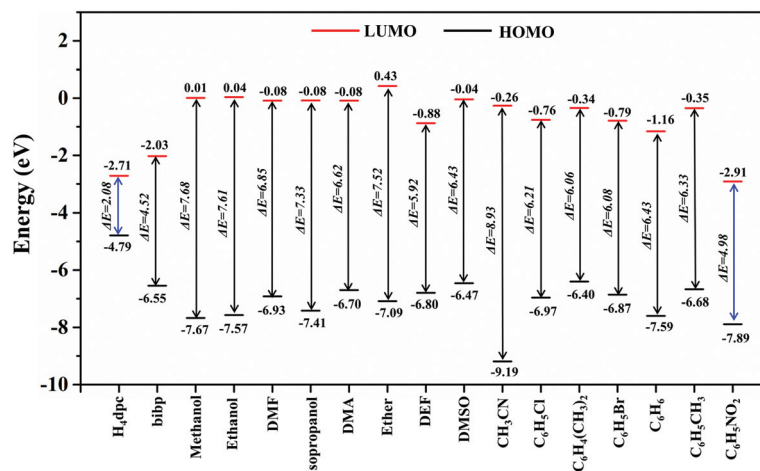
Fig. 7 The calculated HOMO and LUMO energy levels of ligands and the selected analytes.

obtain the recycled Eu-MOF samples. The initial luminescence intensity ($^5D_0 \rightarrow {}^7F_2$) is mainly retained after five cycles and the quenching efficiency of each cycle is over 80%. The results suggest that the Eu-MOF possesses good anti-interference ability and recyclability for sensing applications toward NB (see Fig. 6b). In this work, the sensing selectivity of the chemosensor, Eu-MOF, towards other nitroaromatic compounds was not checked.

Theoretical studies

As per the discussion above, the results of luminescence performances reveal that the Eu-MOF behaves as an efficient and selective chemosensor for the detection of NB with high quenching efficiency. Generally speaking, in Ln-MOFs assembled from antenna ligands, the antenna effect may be inhibited by the interference of the analytes, which may lead to the emission quenching of Ln-MOFs.[46] The luminescence quenching is mainly ascribed to the photoinduced electron transfer (PET) from the donor antenna ligand to the acceptor analytes adsorbed on the surface of the Ln-MOF materials. In the process of electron transfer, at first, the antenna ligand obtains energy from light, and afterwards, the electron transfer occurs from the ground state (HOMO, the highest occupied molecular orbital) to the singlet state (LUMO, the lowest unoccupied molecular orbital).[47,48] The energy levels of the LUMOs of the tested analytes are commonly lower than those in the conduction band (CB) of MOFs, which may serve as intrinsic driving forces for electron transfer from electron-rich MOFs to electron-deficient analytes, and quench the luminescence intensity of MOFs upon excitation. Particularly, as an electron-deficient organic molecule, the LUMO of NB lies at a low-lying π*-type orbital which is stabilized by the conjugation of the −NO$_2$ group, and its energy is below the CB of Eu-MOF.[49–51] In order to gain further insight into the sensing mechanism of the Eu-MOF toward NB, the HOMO and LUMO orbital energies of the antenna ligand (dpc^{4-}) and the tested analytes have been calculated by density functional theory (DFT) at the

B3LYP/6-31G(d) level (Fig. 7). Obviously, the LUMO energy level of the dpc^{4-} ligand (−2.71 eV) is higher than that of NB (−2.91 eV) and lower than those of other organic molecules, which facilitates the excited electron transfer from the ground state of the dpc^{4-} ligand to the LUMO of NB and brings about luminescence quenching.

Selective sensing of cations

The powder sample of the Eu-MOF was finely ground and then dispersed in 1×10^{-3} M DMF solutions of MCl$_x$ (M^{n+} = Cd^{2+}, Zn^{2+}, Na$^+$, Li$^+$, Ba^{2+}, K$^+$, Ca^{2+}, Ni^{2+}, Mn^{2+}, Hg^{2+}, Pb^{2+}, Co^{2+}, Cu$^+$, Al^{3+}, Cu^{2+}, Fe^{3+}), respectively, and ultrasonically stirred for 30 min to form stable M^{n+}@Eu-MOF suspensions, and their luminescence intensities were investigated at an excitation wavelength of 296 nm. As shown in Fig. 8, the luminescence intensities of all suspensions are distinctly dependent on the type of metal ion introduced. Observably, most of the cations exert subtle influences on the emission of the Eu-MOF, whereas, by the introduction of Fe^{3+} or Cu^{2+} cations, the intensities have striking quenching effects, demonstrating that the Eu-MOF exerts a selective luminescence response toward Fe^{3+} and Cu^{2+} and can be regarded as a hopeful candidate to sense both cations. Furthermore, under ultraviolet light of 365 nm, the solution of the Eu-MOF changed distinctly from pink to dark after the addition of Fe^{3+} or Cu^{2+} cations (Fe^{3+}@Eu-MOF or Cu^{2+}@Eu-MOF), respectively, which makes it distinguishable with visible changes in color by the naked eye. Additionally, the PXRD patterns of the Eu-MOF after sensing both metal ions remain intact in comparison with that of the original Eu-MOF sample, which indicates that its framework is still retained (Fig. S7†).

To further explore the correlation between the quenching effect and quantitative sensing capability of the Eu-MOF toward Fe^{3+} and Cu^{2+}, the luminescence titration experiments with an equal concentration of both cations (0–360 μL, 1×10^{-2} M) against the Eu-MOF dispersed in DMF were carried out. As a result, the characteristic emission intensity of the Eu-

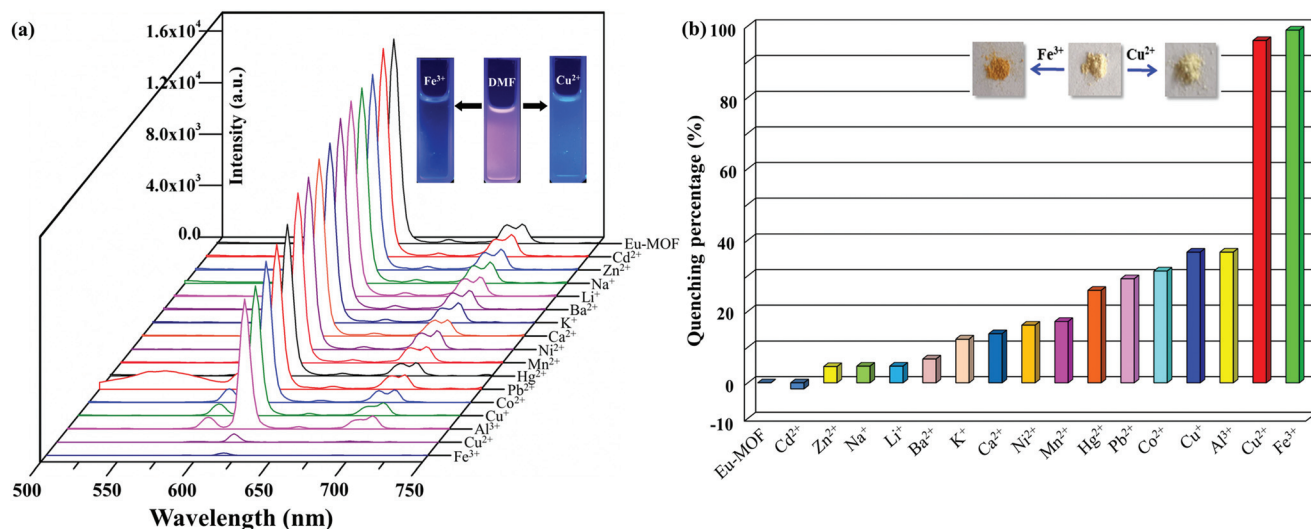**Fig. 8** (a) Luminescence spectra of the Eu-MOF dispersed in different metal cations in DMF solutions (inset: the color changes after adding Fe^{3+}/ Cu^{2+} ions under 365 nm ultraviolet light). (b) Luminescence quenching percentage of the Eu-MOF ($^5D_0 \rightarrow {}^7F_2$) dispersed into different DMF solutions of various cations.

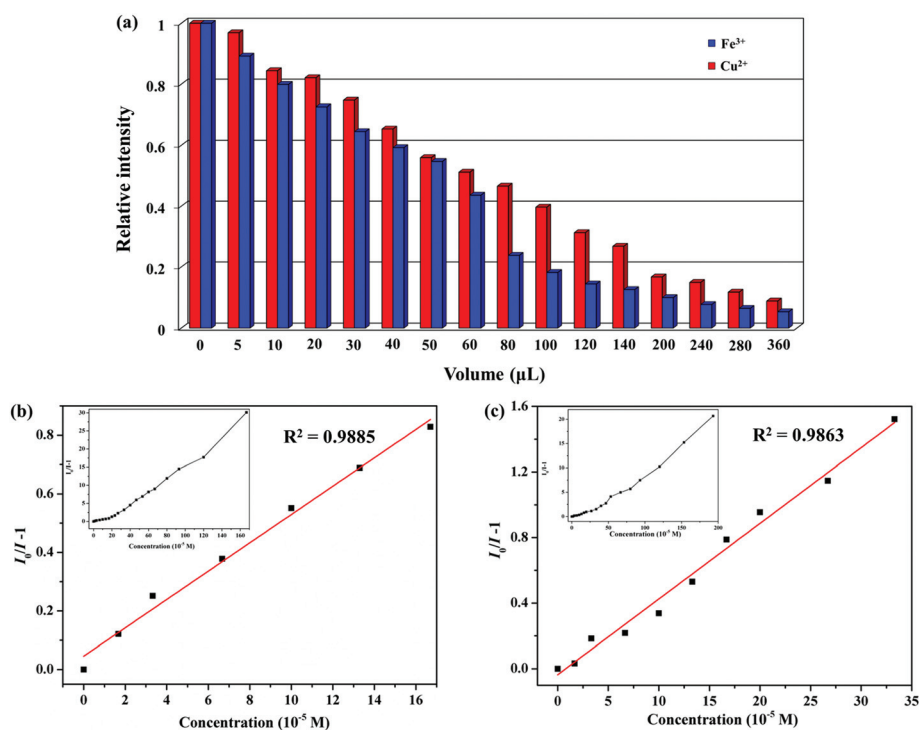**Fig. 9** (a) Concentration-dependent luminescence intensities of the Eu-MOF by addition of different volumes of Fe^{3+} and Cu^{2+} (1×10^{-2} M). Linear SV curves for the Eu-MOF by gradual addition of Fe^{3+} ions (b) and Cu^{2+} ions (c) in DMF solution (inset: nonlinear SV plot of ions).

MOF at 616 nm ($^5D_0 \rightarrow {}^7F_2$) continuously decreased in accordance with the increasing concentration of ions. When the concentration of Fe^{3+} or Cu^{2+} was raised to 360 μL, the luminescence intensity decreased to 94.66% or 91.11%, respectively (see Fig. 9a). Quantitatively, the luminescence intensity *versus* [Fe^{3+}] and [Cu^{2+}] plots show good linear correlation at low con-

centrations (R^2 = 0.9885 for Fe^{3+} and 0.9863 for Cu^{2+}), and are close to the SV equations (Fig. 9b and c). The K_{sv} value of the Eu-MOF for the Fe^{3+} and Cu^{2+} cations was calculated to be 4.84×10^3 M^{-1} and 4.62×10^3 M^{-1}, respectively. According to $3\delta/k$, the LOD values were also obtained as follows: 1.32×10^{-5} M for Fe^{3+} and 2.53×10^{-5} M for Cu^{2+}. However, accompanied

by the increase of concentration, the plots of I_0/I versus concentration of cations deviate from the linear correlation, indicating that the process of luminescence quenching is involved in the coexistence of static and dynamic mechanisms.[52,53]

Moreover, the anti-interference experiments from other metal ions were studied. When Fe^{3+} or Cu^{2+} was slowly added dropwise into various M^{n+}@Eu-MOF suspensions, the luminescence intensity of the Eu-MOF reduced drastically compared to its initial intensity (Fig. S8a and c†), which indicates that the Eu-MOF as the sensor possesses a high selectivity toward Fe^{3+} or Cu^{2+}. The reusability of the material for Fe^{3+} and Cu^{2+} sensing was also examined by using the following procedures. The Eu-MOF powder samples were dispersed in DMF solutions of Fe^{3+} and Cu^{2+} ions, respectively, and treated by ultrasonication for 30 min to form stable suspensions and then washed several times using DMF. Their luminescence intensities were measured at an excitation wavelength of 296 nm. After five cyclic measurements, the emission intensities of the Eu-MOF could not be repeated as strongly as its original intensity, making us infer that this is probably due to the closer weak interactions of Fe^{3+} and Cu^{2+} with N and O atoms from bibp and dpc^{4-} ligands.[54]

Possible mechanism of the sensing system

According to literature reports, the mechanism of MOF luminescence quenching caused by metal ions is mainly attributable to three factors: (1) collapse of the skeleton with the addition of metal cations; (2) cationic-exchange interaction between the tested exterior cations and central metal ions; (3) binding interaction of metal cations with the organic ligands (energy-transfer process).[55–58] To elucidate the possible luminescence quenching mechanism caused by Fe^{3+} or Cu^{2+}, PXRD analysis, inductively coupled plasma-atomic emission spectrometry (ICP-AES), UV-vis spectroscopy and X-ray photoelectron spectroscopy (XPS) against the Eu-MOF and M^{n+}@Eu-MOFs (M^{n+} = Fe^{3+} and Cu^{2+}) were performed, respectively. Consequently, the PXRD patterns of the Eu-MOF and M^{n+}@Eu-MOFs are almost identical, demonstrating that the skeleton of the Eu-MOF remains intact and the luminescence quenching is not attributed to the collapse of the framework. ICP-AES data show that the concentrations of Fe^{3+} or Cu^{2+} in the filtrates decrease to 2.858 or 6.250 mg L^{-1} (the initial concentrations are 5.585 for Fe^{3+} and 6.355 mg L^{-1} for Cu^{2+}) and the adsorption percentages are 48.83% for Fe^{3+} and 16.52% for Cu^{2+}, which may indicate that both guest metal ions interact with the framework of the Eu-MOF material in different degrees (Table S4†). Studies have revealed that the UV-vis absorption spectrum of the Fe^{3+} ion locates in the range of 270 to 350 nm, which is widely overlapped with the excitation wavelength of the Eu-MOF (296 nm), as shown in Fig. S9,† however, the absorption spectrum of the Cu^{2+} ion shows no significant overlap with the excitation spectrum of the Eu-MOF.[59] Taking the crystal structure analysis of the Eu-MOF into account, the cationic exchange interaction between the Fe^{3+} or Cu^{2+} and central Eu(III) cations is difficult to achieve owing to the differences of the electronic effect and the coordi-

nation ability between them. In the 3D framework of the Eu-MOF, uncoordinated carboxyl O or imidazolyl N atoms from dpc^{4-} or bibp ligands may act as Lewis basic sites to be incorporated into Fe^{3+} or Cu^{2+} ions. Meanwhile, the weak interactions between Fe^{3+} or Cu^{2+} and O or N atoms change the electron energy level of ligands and further restrain the process of energy transfer from ligands to Eu(III) centers, leading to a higher quenching efficiency of the Eu-MOF.[60,61] This speculation is also confirmed by the results of XPS measurements. A comparison of the changes in peaks in the XPS spectra before and after treatment with Cu^{2+} shows that the N 1s peaks shift from free nitrogen atoms at 398.88 eV and 401.18 eV to 399.48 and 401.08 eV, whereas the O 1s peaks remain unchanged, which further confirms the weak interaction between the N atoms and Cu^{2+}. Similarly, as for Fe^{3+}, the N 1s peaks shift from 398.88 and 401.18 eV to 399.58 and 401.48 eV, while the O 1s peaks shift from 531.38 and 532.78 eV to 531.78 and 532.98 eV, respectively, which may result from the weak interactions of Fe^{3+} with the N and O atoms from the bibp and dpc^{4-} ligands (Fig. 10).[62–64] Such interactions may disturb the singlet and triplet excited states of ligands and reduce the energy transfer efficiency from the ligands to the Eu(III) centers and thus lead to the luminescence quenching of the Eu-MOF.[65,66]

Selective sensing of anions

Simultaneously, we also analyzed the responses of the Eu-MOF toward common anions by adopting a similar strategy of cation sensing. The as-prepared sample of the Eu-MOF was dispersed in different DMF solutions containing 1×10^{-3} M Na_nX (X = Cl^-, Br^-, I^-, OH^-, CO_3^{2-}, HCO_3^-, NO_3^-, NO_2^-, SO_4^{2-}, PO_4^{3-}, HPO_4^{2-}, $H_2PO_4^-$, $Cr_2O_7^{2-}$) to investigate their influences on the emission intensities at an excitation wavelength of 296 nm. As depicted in Fig. 11, the intensity for the $^5D_0 \rightarrow {}^7F_2$ at 616 nm transition of the Eu-MOF is significantly decreased after the addition of a trace amount of $Cr_2O_7^{2-}$, and the quenching efficiency comes up to 96.03%. However, the intensities of the Eu-MOF merely weaken indistinctively in the presence of all the other tested anions. Therefore, the Eu-MOF may be a potential chemosensor to distinguish $Cr_2O_7^{2-}$ from the above-mentioned common anions. Remarkably, under the irradiation at 365 nm, the process of sensing toward $Cr_2O_7^{2-}$ is accompanied by changes in color, which can be visibly distinguished by the naked eye, as illustrated in Fig. 11a (inset).

In order to evaluate the relationship between concentration and intensity, luminescence titration measurements of the Eu-MOF were further performed by the gradual addition of $Cr_2O_7^{2-}$ (1×10^{-2} M) into a solution of DMF containing the Eu-MOF. As expected, the emission intensity at 616 nm ($^5D_0 \rightarrow {}^7F_2$) of the Eu-MOF gradually weakened along with the increasing concentrations of $Cr_2O_7^{2-}$. The Stern–Volmer (SV) curve for $Cr_2O_7^{2-}$ exhibits a good linear correlation between the luminescence intensity and the concentration of $Cr_2O_7^{2-}$ at low concentrations (R^2 = 0.9927) (Fig. 12), which affords a value of K_{sv} = 3.97×10^3 M^{-1}, and the LOD is calculated to be 1.01×10^{-5} M. The plot of titration experiment deviates from linearity as
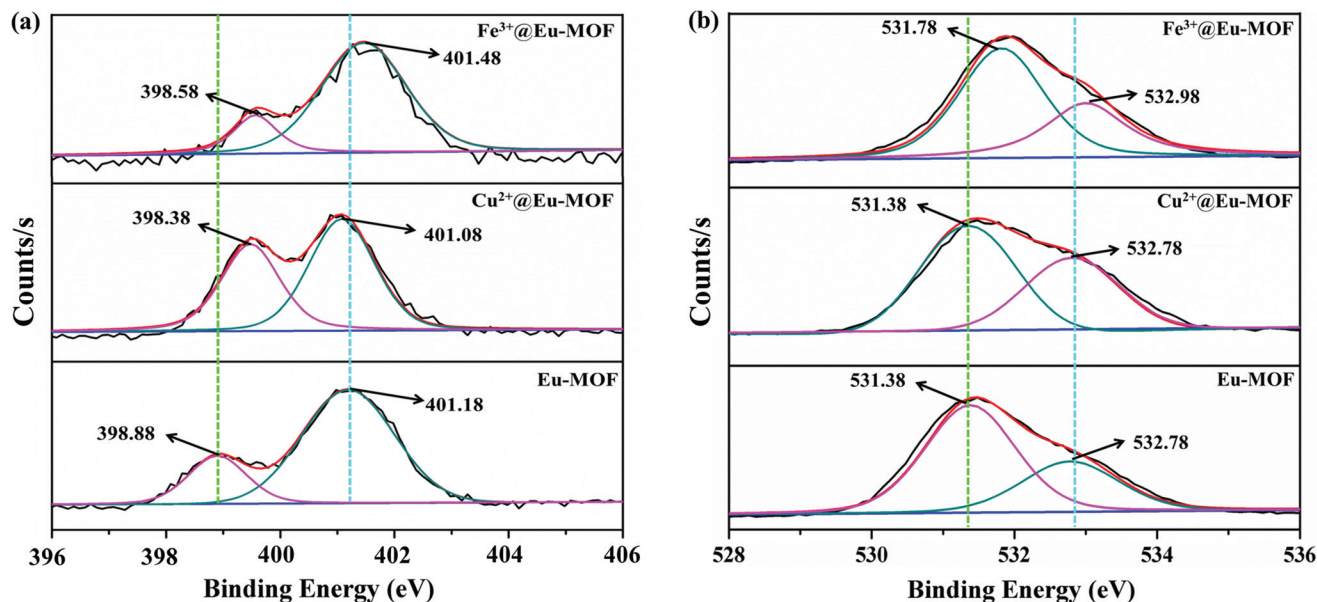
Fig. 10   (a) N 1s XPS spectra of Eu-MOF, Cu^{2+}@Eu-MOF and Fe^{3+}@Eu-MOF. (b) O 1s XPS spectra of Eu-MOF, Cu^{2+}@Eu-MOF and Fe^{3+}@Eu-MOF.
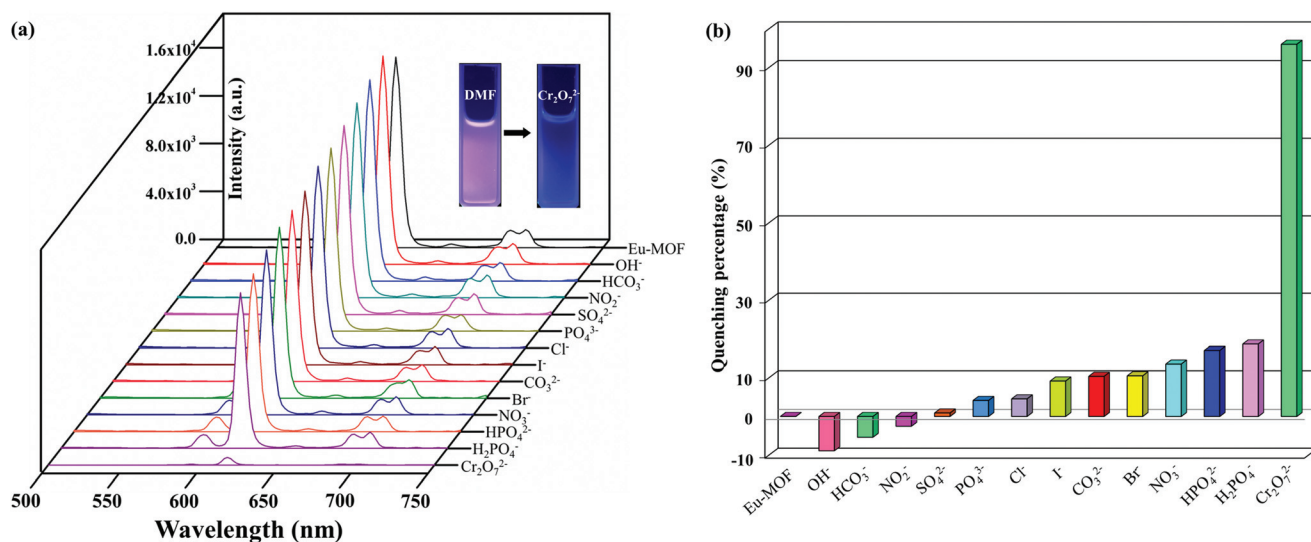

Fig. 11   (a) Luminescence spectra of the Eu-MOF dispersed in DMF solutions containing different anions (inset: the color changes after adding Cr$_2$O$_7^{2-}$ under 365 nm ultraviolet light). (b) Luminescence quenching percentage of the Eu-MOF ($^5D_0 \rightarrow {}^7F_2$) dispersed into different DMF solutions of various anions.

the concentration increases, illustrating that both static and dynamic quenching processes occur synchronously.[67,68]

To evaluate the sensing selectivity of the interfering analytes, 300 μL Cr$_2$O$_7^{2-}$ DMF solution (1×10^{-2} M) was injected into other anion suspensions, respectively, and as expected, each luminescence intensity was quenched sharply (Fig. S9a†). Simultaneously, the cyclic experiment indicates that the emission intensity can be roughly restored after five recycles (Fig. S10b†). The above results demonstrate the good recyclability and anti-interference ability of the Eu-MOF for detecting Cr$_2$O$_7^{2-}$.

The mechanism of luminescence quenching of the Eu-MOF caused by Cr$_2$O$_7^{2-}$ was also investigated. Firstly, the PXRD pattern of Cr$_2$O$_7^{2-}$@Eu-MOF was in good agreement with that of the original Eu-MOF sample, suggesting that the framework of the Eu-MOF remained unchanged after its incorporation with Cr$_2$O$_7^{2-}$. Apparently, the quenching mechanism based on the collapse of the architecture of the Eu-MOF may be eliminated (see Fig. S11†). Secondly, the UV-vis absorption spectrum of Cr$_2$O$_7^{2-}$ situates within the range of 230–500 nm, which overlaps with the excitation peak of the Eu-MOF (296 nm) (Fig. S12†). Consequently, the excitation light can be
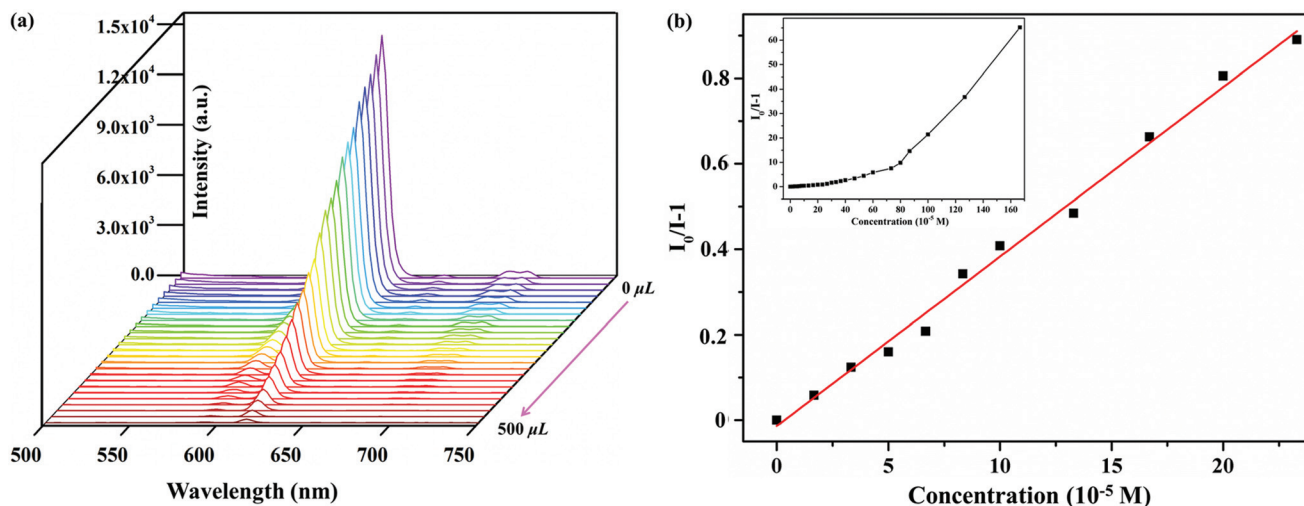
Fig. 12 (a) Concentration-dependent luminescence intensities of the Eu-MOF by addition of different volumes of $Cr_2O_7^{2-}$ (1×10^{-2} M). (b) Linear SV curve for $Cr_2O_7^{2-}$ (inset: nonlinear SV plot of $Cr_2O_7^{2-}$).

partially absorbed by $Cr_2O_7^{2-}$ anions, which inhibits the energy transfer from the ligands to the Eu(III) centers efficiently, and eventually induces the luminescence quenching to some degree.[69,70]

Conclusions

In summary, a series of 3D lanthanide-based metal–organic frameworks (Ln-MOFs) with the general formula {[Ln(dpc)(2H₂O)]·(Hbibp)$_{0.5}$}$_n$ [[H₄dpc = 2-(3′,4′-dicarboxylphenoxy)isophthalic acid, bibp = 4,4′-bis(imidazolyl) biphenyl, Ln = La(I), Ce(II), Pr(III), Nd(IV), Sm(V), and Eu(VI)], have been hydrothermally assembled and characterized. Single-crystal X-ray diffraction indicates that **I–VI** are isostructural and the lanthanide center is nine-coordinated with a distorted tetrakaidecahedral configuration. Remarkably, the luminescence and sensing properties of **I–VI** were studied systematically, indicating that Eu-MOF (**VI**) exhibits characteristic emissions of the Eu(III) ion and behaves as a multi-responsive luminescent sensor toward Fe^{3+}, Cu^{2+}, $Cr_2O_7^{2-}$, and nitrobenzene with high sensitivity, selectivity, stability and anti-interference ability even in the presence of other ions or molecules based on their great luminescence quenching efficiencies. In addition, Eu-MOF (**VI**) demonstrates excellent luminescence stability and retains its structural integrity within the pH range of 2–12 in an aqueous solution and its solid sample maintains high thermodynamic stability up to 320 °C, which facilitate its practical applications. Furthermore, as evidenced by density functional theory (DFT), PXRD analysis, inductively coupled plasma-atomic emission spectrometry (ICP-AES), UV-vis spectroscopy and X-ray photoelectron spectroscopy (XPS), the possible luminescence sensing mechanisms for the above analytes have been discussed in detail. The present work may provide a practical strategy to design and assemble Ln-MOFs as multifunctional luminescent chemosensors for the sensing of environ-

mental contaminants. In this work, the sensing selectivity of the chemosensor, Eu-MOF, towards other nitroaromatic compounds such as nitrophenol (NP), nitromethane (NM), 2,4-dinitro toluene (2,4-DNT), 2,6-dinitro toluene (2,6-DNT), 3,5-dinitro benzoic acid (3,5-DNBA), 4-nitrobenzoic acid (4-NBA) 2,4-dinitrophenol (DNP), 2,4,6-trinitrophenol (TNP) *etc.* was not checked and this will be our further work in the future.

Conflicts of interest

The authors declare no competing financial interest.

Acknowledgements

References

1 Y. Zhao, X. Y. Xu, L. Qiu, X. J. Kang, L. L. Wen and B. G. Zhang, *ACS Appl. Mater. Interfaces*, 2017, **9**, 15164–15175.

2 K. Müller-Buschbaum, F. Beuerle and C. Feldmann, *Microporous Mesoporous Mater.*, 2015, **216**, 171–199.

3 H. Wang, W. P. Lustig and J. Li, *Chem. Soc. Rev.*, 2018, **47**, 4729–4756.

4 D. Kukkara, K. Vellingiric, K. H. Kimb and A. Deepd, *Sens. Actuators, B*, 2018, **273**, 1346–1370.

5 Y. Y. Jia, Y. H. Zhang, J. Xu, R. Feng, M. S. Zhang and X. H. Bu, *Chem. Commun.*, 2015, **51**, 17439–17442.

6 D. Zhao, X. H. Liu, Y. Zhao, P. Wang, Y. Liu, M. Azam, S. I. Al-Resayes, Y. Lu and W. Y. Sun, *J. Mater. Chem. A*, 2017, **5**, 15797–15807.

7 B. H. Fan, J. Wei, X. X. Ma, X. X. Bu, N. N. Xing, Y. Pan, L. Zheng and W. Guan, *Ind. Eng. Chem. Res.*, 2016, **55**, 2267–2271.

8 L. Guo, Y. Liu, R. M. Kong, G. Chen, Z. Liu, F. L. Qu, L. Xia and W. H. Tan, *Anal. Chem.*, 2019, **91**, 12453–12460.

9 L. Li, M. J. Hou, L. Cao, Y. Xia, Z. G. Shen and Z. B. Hu, *Environ. Exp. Bot.*, 2018, **155**, 313–320.

10 Y. Zhang and B. Yan, *Talanta*, 2019, **197**, 291–298.

11 G. Q. Niu, C. Si, J. C. Jiao, Q. X. Han, M. F. Guo and M. X. Li, *J. Alloys Compd*, 2020, **830**, 154696.

12 W. Liu, Y. L. Wang, Z. L. Bai, Y. X. Li, Y. X. Wang, L. H. Chen, L. Xu, J. D. Wu, Z. F. Chai and S. A. Wang, *ACS Appl. Mater. Interfaces*, 2017, **9**, 16448–16457.

13 S. Rapti, D. Sarma, S. A. Diamantis, E. Skliri, G. S. Armatas, A. C. Tsipis, Y. S. Hassan, M. Alkordi, C. D. Malliakas, M. G. Kanatzidis, T. Lazarides, J. C. Plakatouras and M. J. Manos, *J. Mater. Chem. A*, 2017, **5**, 14707–14719.

14 H. M. He, S. H. Chen, D. Y. Zhang, R. Hao, C. Zhang, E. C. Yang and X. J. Zhao, *Dalton Trans.*, 2017, **46**, 13502–13509.

15 L. R. Yang, C. Lian, X. F. Li, Y. Y. Han, L. L. Yang, T. Cai and C. Y. Shao, *ACS Appl. Mater. Interfaces*, 2017, **9**, 17208–17217.

16 D. X. Ma, B. Y. Li, X. J. Zhou, Q. Zhou, K. Liu, G. Zeng, G. H. Li, Z. Shi and S. H. Feng, *Chem. Commun.*, 2013, **49**, 8964–8966.

17 D. M. Chen, X. Z. Ma, W. Shi and P. Cheng, *Cryst. Growth Des.*, 2015, **15**, 3999–4004.

18 S. Y. Lee, K. K. Y. Yuen, K. A. Jolliffe and J. Y. Yoon, *Chem. Soc. Rev.*, 2015, **44**, 1749–1762.

19 J. J. Jiang, Z. Y. Lu, M. X. Zhang, J. G. Duan, W. W. Zhang, Y. Pan and J. F. Bai, *J. Am. Chem. Soc.*, 2018, **140**, 17825–17829.

20 X. Yang, X. Lin, Y. Zhao, Y. S. Zhao and D. Yan, *Angew. Chem., Int. Ed.*, 2017, **56**, 7853–7857.

21 A. Schoedel, M. Li, D. Li, M. O'Keeffe and O. M. Yaghi, *Chem. Rev.*, 2016, **116**, 12466–12535.

22 Y. J. Cui, B. L. Chen and G. D. Qian, *Coord. Chem. Rev.*, 2014, **273**, 76–86.

23 H. C. Zhou, J. R. Long and O. M. Yaghi, *Chem. Rev.*, 2012, **112**, 673–674.

24 B. Yan, *Acc. Chem. Res.*, 2017, **50**, 2789–2798.

25 Y. L. Li, Y. Zhao, P. Wang, Y. S. Kang, Q. Liu, X. D. Zhang and W. Y. Sun, *Inorg. Chem.*, 2016, **55**, 11821–11830.

26 L. R. Yang, H. M. Zhang, Q. Q. You, L. Z. Wu, L. Liu and S. Song, *CrystEngComm*, 2013, **15**, 7505–7514.

27 Q. G. Zhai, X. H. Bu, X. Zhao, D. S. Li and P. Y. Feng, *Acc. Chem. Res.*, 2017, **50**, 407–417.

28 A. Karmakar, P. Samanta, A. V. Desai and S. K. Ghosh, *Acc. Chem. Res.*, 2017, **50**, 2457–2469.

29 N. N. Sun and B. Yan, *Sens. Actuators, B*, 2018, **261**, 153–160.

30 M. Kumar, L. H. Wu, M. Kariem, A. Franconetti, H. N. Sheikh, S. J. Liu, S. C. Sahoo and A. Frontera, *Inorg. Chem.*, 2019, **58**, 7760–7774.

31 H. Y. Li, H. Xu, S. Q. Zang and T. C. Mak, *Chem. Commun.*, 2016, **52**, 525–528.

32 C. H. Zhang, H. Z. Shi, L. B. Sun, Y. Yan, B. L. Wang, Z. Q. Liang, L. Wang and J. Y. Li, *Cryst. Growth Des.*, 2018, **18**, 7683–7689.

33 A. D. G. Firmino, F. Figueira, J. P. C. Tomé, F. A. A. Paz and J. Rocha, *Coord. Chem. Rev.*, 2018, **355**, 133–149.

34 S. Yao, D. M. Wang, Y. Cao, G. H. Li, Q. S. Huo and Y. L. Liu, *J. Mater. Chem. A*, 2015, **3**, 16627–16632.

35 L. Z. Liu, Y. Wang, R. Y. Lin, Z. Z. Yao, Q. J. Lin, L. H. Wang, Z. J. Zhang and S. C. Xiang, *Dalton Trans.*, 2018, **47**, 16190–16196.

36 J. J. Huang, J. H. Yu, F. Q. Bai and J. Q. Xu, *Cryst. Growth Des.*, 2018, **18**, 5353–5364.

37 Y. Du, J. W. Liu, C. Y. Shao and L. R. Yang, *J. Alloys Compd.*, 2019, **781**, 904–912.

38 Y. Liu, J. J. Ma, C. Xu, Y. Yang, M. F. Xia, H. E. Jiang and W. S. Liu, *Dalton Trans.*, 2018, **47**, 13543–13549.

39 Y. Lu and B. Yan, *Chem. Commun.*, 2014, **50**, 13323–13326.

40 Z. Cui, X. Y. Zhang, S. Liu, L. Zhou, W. L. Li and J. P. Zhang, *Inorg. Chem.*, 2018, **57**, 11463–11473.

41 Q. S. Wang, J. J. Li, M. N. Zhang and X. Li, *Sens. Actuators, B*, 2018, **258**, 358–364.

42 X. Y. Xu and B. Yan, *ACS Appl. Mater. Interfaces*, 2014, **7**, 721–729.

43 Y. P. Wu, G. W. Xu, W. W. Dong, J. Zhao, D. S. Li, J. Zhang and X. H. Bu, *Inorg. Chem.*, 2017, **56**, 1402–1411.

44 M. L. Han, G. X. Wen, W. W. Dong, Z. H. Zhou, Y. P. Wu, J. Zhao, D. S. Li, L. F. Ma and X. H. Bu, *J. Mater. Chem. C*, 2017, **5**, 8469–8474.

45 L. L. Ren, Y. Y. Cui, A. L. Cheng and E. Q. Gao, *J. Solid State Chem.*, 2019, **270**, 463–469.

46 D. M. Chen, J. Y. Tian and C. S. Liu, *Inorg. Chem.*, 2016, **55**, 8892–8897.

47 S. Y. Wu, Y. N. Lin, J. W. Liu, W. Shi, G. M. Yang and P. Cheng, *Adv. Funct. Mater.*, 2018, **28**, 1707169.

48 D. M. Chen, N. N. Zhang, C. S. Liu and M. Du, *J. Mater. Chem. C*, 2017, **5**, 2311–2317.

49 H. R. Fu, Y. Zhao, T. Xie, M. L. Han, L. F. Ma and S. Q. Zang, *J. Mater. Chem. C*, 2018, **6**, 6440–6448.

50 X. Z. Song, S. Y. Song, S. N. Zhao, Z. M. Hao, M. Zhu, X. Meng, L. L. Wu and H. J. Zhang, *Adv. Funct. Mater.*, 2014, **24**, 4034–4041.

51 D. S. Zhang, Q. Gao, Z. Chang, X. T. Liu, B. Zhao, Z. H. Xuan, T. L. Hu, Y. H. Zhang, J. Zhu and X. H. Bu, *Adv. Mater.*, 2018, **30**, 1804715.

52 Z. Sun, Y. G. Li, Y. Ma and L. C. Li, *Dyes Pigm.*, 2017, **146**, 263–271.

53 W. Yan, C. L. Zhang, S. G. Chen, L. J. Han and H. G. Zheng, *ACS Appl. Mater. Interfaces*, 2017, **9**, 1629–1634.

54 W. Z. Wang, N. Gong, H. Yin, B. Zhang, P. Guo, B. Liu and Y. Y. Wang, *Inorg. Chem.*, 2019, **58**, 10295–10303.

55 B. L. Chen, L. B. Wang, Y. Q. Xiao, F. R. Fronczek, M. Xue, Y. J. Cui and G. D. Qian, *Angew. Chem., Int. Ed.*, 2009, **48**, 500–503.

56 S. Dang, E. Ma, Z. M. Sun and H. J. Zhang, *J. Mater. Chem.*, 2017, **22**, 16920–16926.

57 C. X. Yang, H. B. Ren and X. P. Yan, *Anal. Chem.*, 2013, **85**, 7441–7446.

58 P. C. Rao and S. Mandal, *Inorg. Chem.*, 2018, **57**, 11855–11858.

59 Y. Liu, L. N. Ma, W. J. Shi, Y. K. Lu, L. Hou and Y. Y. Wang, *J. Solid State Chem.*, 2019, **277**, 636–647.

60 H. J. Zhang, R. Q. Fan, W. Chen, J. Z. Fan, Y. W. Dong, Y. Song, X. Du, P. Wang and Y. L. Yang, *Cryst. Growth Des.*, 2016, **16**, 5429–5440.

61 J. N. Xiao, J. J. Liu, X. C. Gao, G. F. Ji, D. B. Wang and Z. L. Liu, *Sens. Actuators, B*, 2018, **269**, 164–172.

62 S. L. Yang, Y. Y. Yuan, P. P. Sun, T. Lin, C. X. Zhang and Q. L. Wang, *New J. Chem.*, 2018, **42**, 20137–20143.

63 J. Luo, B. S. Liu, X. R. Zhang and R. T. Liu, *J. Mol. Struct.*, 2019, **1177**, 444–448.

64 Z. Y. Zhan, X. Y. Liang, X. L. Zhang, Y. J. Jia and M. Hu, *Dalton Trans.*, 2019, **48**, 1786–1794.

65 Q. S. Zhang, J. Wang, A. M. Kirillov, W. Dou, C. Xu, C. L. Xu, L. Z. Yang, R. Fang and W. S. Liu, *ACS Appl. Mater. Interfaces*, 2018, **10**, 23976–23986.

66 X. N. Wang, J. L. Li, C. G. Jiang, P. Hu, B. Li, T. L. Zhang and H. C. Zhou, *Chem. Commun.*, 2018, **54**, 13271–13274.

67 J. Y. Zou, L. Li, S. Y. You, Y. W. Liu, H. M. Cui, J. Z. Cui and S. W. Zhang, *Dalton Trans.*, 2018, **47**, 15694–15702.

68 Y. L. Gai, Q. Guo, X. Y. Zhao, Y. Chen, S. Liu, Y. Zhang, C. X. Zhuo, C. Yao and K. C. Xiong, *Dalton Trans.*, 2018, **47**, 12051–12055.

69 M. M. Xu, X. J. Kong, T. He, X. Q. Wu, L. H. Xie and J. R. Li, *Inorg. Chem.*, 2018, **57**, 14260–14268.

70 X. J. Zhang, F. Z. Su, D. M. Chen, Y. Peng, W. Y. Guo, C. S. Liu and M. Du, *Dalton Trans.*, 2019, **48**, 1843–1849.